



HAL
open science

Room-Temperature Sintering of Amorphous Thiophosphate Solid Electrolyte (Li_3PS_4): Coupling Morphological Evolution to Electrochemical Properties

Patrice Perrenot, Adrien Fauchier-Magnan, Marta Mirolo, Lauréline Lecarme, Pierre-Henri Jouneau, Adrien Boulineau, Pascale Bayle-Guillemaud, Claire Villevieille

► To cite this version:

Patrice Perrenot, Adrien Fauchier-Magnan, Marta Mirolo, Lauréline Lecarme, Pierre-Henri Jouneau, et al.. Room-Temperature Sintering of Amorphous Thiophosphate Solid Electrolyte (Li_3PS_4): Coupling Morphological Evolution to Electrochemical Properties. *Advanced Functional Materials*, 2024, 34 (2), 10.1002/adfm.202310739 . hal-04222513

HAL Id: hal-04222513

<https://hal.science/hal-04222513>

Submitted on 29 Sep 2023

HAL is a multi-disciplinary open access archive for the deposit and dissemination of scientific research documents, whether they are published or not. The documents may come from teaching and research institutions in France or abroad, or from public or private research centers.

L'archive ouverte pluridisciplinaire **HAL**, est destinée au dépôt et à la diffusion de documents scientifiques de niveau recherche, publiés ou non, émanant des établissements d'enseignement et de recherche français ou étrangers, des laboratoires publics ou privés.

Room-Temperature Sintering of Amorphous Thiophosphate Solid Electrolyte (Li_3PS_4): Coupling Morphological Evolution to Electrochemical Properties

Patrice Perrenot, Adrien Fauchier-Magnan, Marta Mirolo, Lauréline Lecarme, Pierre-Henri Jouneau, Adrien Boulineau, Pascale Bayle-Guillemaud, and Claire Villevieille*

Thiophosphate solid electrolytes (Li_3PS_4 , hereafter denoted LPS) have the advantage of presenting a reasonable ionic conductivity at room temperature ($\approx 0.3 \text{ mS cm}^{-1}$) and an easy manufacturing, meaning that they can be sintered at room temperature. Unfortunately, during cycling, several chemo-mechanical degradations quite often attributed to the electrochemical activities occur, but they could also be linked to the sintering process. To date, a fundamental understanding of room-temperature sintering and its impact on the microstructure, the ionic conductivity, and the link between electrochemistry and structure/morphology remains imprecise. In this study, a comprehensive study of homemade amorphous 75% $\text{Li}_2\text{S} - 25\% \text{P}_2\text{S}_5$ (Li_3PS_4) is presented, investigating the influence of pressure and time of room temperature sintering. Focused ion beam-scanning electron microscopy coupled to electrochemical techniques such as electrochemical impedance spectroscopy, Li plating/ stripping and coupled to structural techniques such as wide-angle X-ray scattering are used to establish the link between structure, morphology, and electrochemical properties. It is demonstrated that the room temperature sintering of solid electrolytes is not that trivial and that the commonly accepted rule “less porosity = better ionic conductivity” is not always true and that many additional parameters should be considered to properly sinter the solid electrolyte.

issues in the current Li-ion batteries, solid electrolytes (SE) could allow the use of lithium metal anode ($C_{\text{th}} = 3860 \text{ mAh}\cdot\text{g}^{-1}$) with the promise to increase the energy density and prolong cycle life.^[1,2] This could only be feasible if one can control the multiple interfaces (including the solid/solid interface) that cause tremendous issues like electro-chemo-mechanical processes.^[3,4] However, in the literature, a link is missing. All degradation processes are related to the cycling behavior that is supposed to cause all the aging processes, but it could be coming also from an earlier stage, the sintering of the solid electrolyte/composite electrode. In this field, improvements will emerge from the understanding and tailoring of particular microstructures and morphologies.^[5,6] Indeed, it is well known that Li-ion transport is optimal in solid-state batteries if the tortuosity is reduced to unity in the full multi-materials 3D system. The study of the 3D morphology and/or microstructure of the solid


electrolyte could bring crucial information to improve their overall electrochemical performance. The main issue with those investigations is the lack of proper methodology. Commonly, a cross-section of the solid electrolyte is created exposing

1. Introduction

Solid state batteries (SSB) are believed to be the next-generation batteries' breakthrough. Besides the reduction of fire hazard

P. Perrenot, A. Boulineau
Université Grenoble Alpes
CEA
Liten
DTNM
Grenoble 38000, France

A. Fauchier-Magnan, L. Lecarme, C. Villevieille
Université Grenoble Alpes
Université Savoie Mont Blanc
CNRS
Grenoble INP
LEPMI
Grenoble 38000, France
E-mail: claire.villevieille@grenoble-inp.fr
M. Mirolo
European Synchrotron Radiation Facility (ESRF)
Experimental division
71 Avenue des Martyrs, Grenoble 38000, France
P.-H. Jouneau, P. Bayle-Guillemaud
Université Grenoble Alpes
CEA
IRIG
Grenoble 38000, France

 The ORCID identification number(s) for the author(s) of this article can be found under <https://doi.org/10.1002/adfm.202310739>

© 2023 The Authors. Advanced Functional Materials published by Wiley-VCH GmbH. This is an open access article under the terms of the Creative Commons Attribution License, which permits use, distribution and reproduction in any medium, provided the original work is properly cited.

DOI: 10.1002/adfm.202310739

the interior of the electrolyte either by cracking the pellet or by using a focused-ion beam-scanning electron microscopy (FIB-SEM).^[7] These methods give a realistic estimation of the overall porosity by assuming an isotropic microstructure. However, this approach has clear limitations because i) uniaxial sintering could give rise to anisotropy in the microstructure and ii) 2D analysis tends to give limited information when considering 3D complex microstructure. Strong from this observation, many studies are now conducted using 3D techniques such as FIB-SEM tomography or X-ray computed tomography. To date, most of them are mainly focused on the composite electrodes after cycling.^[8–10]

The solid electrolyte used as a separator deserves the same investigation to ensure it is not responsible for premature cell failure in case of poor sintering. Thiophosphate solid electrolytes have a clear advantage over their ceramic substitutes; their capability to be sintered at room temperature. As follows, the compaction process is rarely complete at room temperature (RT) and an amount of porosity remains, affecting as a consequence the electrochemical properties, especially the Li-ion transport, and the mechanical stability.^[11] Some studies reported that a heat treatment on the amorphous form of Li_3PS_4 improves the densification and reduces the porosity leading to higher critical current density.^[12,13] Taken into consideration that amorphous sulfide-based solid electrolytes could deteriorate at relatively low temperatures ($\approx 180^\circ\text{C}$),^[14,15] the shaping of the powder could be done exclusively by pressure to ensure keeping the ionic conductivity parameter. It has already been reported in the literature with X-ray computational tomography that, for the $\text{Li}_6\text{PS}_5\text{Cl}_{1-x}\text{I}_x$ solid electrolyte, high applied pressure can increase the contact area, reduce voids, and thus improve ionic conductivity.^[16] The structure of the electrolyte is also an important parameter, for example, the optimum pellet pressure is different for amorphous or crystalline sulfide-based solid electrolytes and has an impact on the stacking pressure required to achieve high ionic conductivity.^[17] However, the impact of pressing time at room temperature on the sintering and degradation process has not been studied to the best of our knowledge.

To date, only a limited number of papers approach exclusively the effect of sintering of sulfide-based electrolytes and the impact on their microstructure and morphology.^[18] This missing piece of the puzzle is rather surprising considering the number of investigations dedicated to failure mechanisms. As an example, it has been shown that lithium dendrites could grow across a sulfide-based electrolyte separator and create a short circuit,^[19,20] and that the remaining porosity could be enhancing this process highlighting, once again, the importance of proper sintering of the solid electrolyte.^[11,21]

In this paper, we varied the room temperature sintering parameters (pressure and time) on amorphous 75% Li_2S – 25% P_2S_5 (Li_3PS_4 , hereafter denoted LPS) using an uniaxial press to monitor the morphological and electrochemical evolutions and find correlations between them. FIB-SEM measurements are performed and thoroughly quantified to assess the impact of the sintering parameter on several metrics (local thickness, porosity size dependency, geodesic maps, etc.). Those metrics will help us describe the lithium paths and their blocking point respectively prior to being compared to their electrochemical properties. The structure of the solid electrolyte will then be assessed by an in situ in-depth profiling using an advanced wide-angle X-ray scattering

(WAXS) technique to check that no structural change occurred during sintering. Finally, a correlation will be made between ion transport properties (geodesic distance) and ionic conductivity, whereas geometric tortuosity will be linked to mechanical stability assessed by lithium plating/stripping test.

2. Physical and Chemical Characterization

The amorphous Li_3PS_4 (LPS) material used in this study is obtained by ball milling of the precursors Li_2S and P_2S_5 used in stoichiometric amounts (see Experimental Section for more detail). WAXS was used to ensure that the synthesized material is amorphous. As seen in Figure S1, Supporting Information, the diffractogram possesses only slight impurity peaks (Li_2S phase [ICSD 01-077-2145]) and an amorphous phase. As the material is air sensitive, we made it react with air and moisture to see the changes occurring in the LPS structure, as shown in the X-ray diffractogram in Figure S1, Supporting Information. This experiment helps us to ensure that the data collected through this paper are not a result of air/moisture contamination, since it is easy to track it by X-ray diffraction (XRD). Due to the high sensitivity of LPS material with air/moisture and with most of the solvents, it is difficult to estimate the particle size distribution of the powder by conventional techniques such as a particle size analyzer. Thus, it was estimated by means of scanning electron microscope (SEM) images and image analysis as shown in Figure S2, Supporting Information. From this analysis, it seems that the median diameter D50 (value of the particle diameter at 50% in the cumulative distribution) of the powder is between 2.5 and 4 μm from the minimum and maximum Feret diameter histogram respectively. This result might be slightly overestimated for two reasons: i) the LPS particles tend to agglomerate to form clusters that are hardly separable owing to their adhesive quality and ii) the image analysis procedures are not separating all the particles as seen on the backscattered electron image with the magenta overlay. Nonetheless, this method gives a satisfactory estimation of the size of the particles before the room-temperature sintering process.

3. Shaping/Room-Temperature Sintering

3.1. Densification

To ensure proper Li-ion transport in solid-state batteries, the room temperature sintering of the solid electrolyte should be optimized to reduce as much as possible the porosity. FIB-SEM tomography was performed on four different samples to check the impact of the pressure applied and the time this pressure should be applied. For a fair comparison, the same set-up and the same amount of solid electrolyte were sintered, and all tomograph images were performed in the same region of the solid electrolyte pellet (500 μm from the center of the pellets, Figure S3, Supporting Information) and approximately equivalent volume was acquired ($20 \times 20 \times 20 \mu\text{m}^3$) with a voxel size of 20 nm. This methodology will have the benefit that the tomography volumes can be compared with each other. As can be seen in Figure 1, it seems that the most important parameter to control is the pressure as, at higher pressure (510 MPa), the solid electrolyte is way denser (compacity $\approx 97\%$) than the

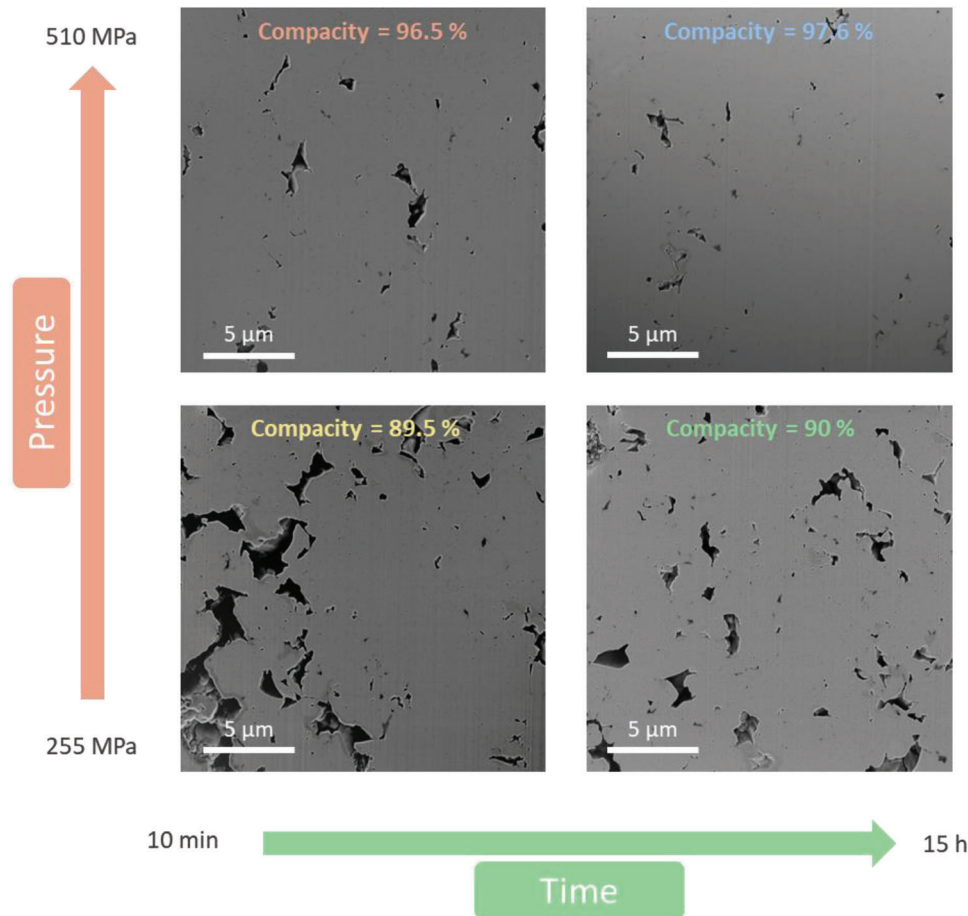


Figure 1. Secondary electron image extracted from the FIB-SEM stacks for the four different samples as a function of applied time/pressure.

one at 255 MPa (compaction \approx 90%). As such, it looks like pressing for a longer time is only reducing marginally the amount of porosity. Unfortunately, the images here are only 2D and cannot reflect the behavior of the solid electrolyte in 3D, thus image reconstructions in 3D using algorithms are crucial to point out differences.

Several parameters can be extracted from the image analysis (Table 1), the first one being the densification of the solid electrolyte. Here, we dissociate the contribution from the Li_3PS_4 solid electrolyte from the one of Li_2S , considered an impurity with poor ionic conductivity at room temperature, thus behaving like a pore for Li-ion transport. When sintered at 255 MPa for a short time

Table 1. Summary of the results obtained from the investigations led on the FIB-SEM 3D reconstruction. Details about the calculation can be found in the Experimental Section.

	255 MPa, 10 min	255 MPa, 15 h	510 MPa, 10 min	510 MPa, 15 h
LPS volume fraction [%]	89.3	89.9	96.4	97.3
Li_2S volume fraction [%]	0.2	0.1	0.1	0.3
Porosity volume fraction [%]	10.5	10.0	3.5	2.4
τ +/-y tortuosity in LPS + Li_2S	1.032	1.030	1.009	1.007
Average local thickness in LPS + Li_2S [μm]	0.96	0.99	1.28	1.21
Std dev. local thickness in LPS + Li_2S [μm]	0.39	0.40	0.50	0.42
Minimum length to connect top and bottom through porosities (μm)	22.06	22.60	25.48	X
Minimum/maximum tortuosity to connect through porosities	1.103 – 1.475	1.130 – 1.454	1.274 – 1.537	X

(10 min), an average densification of $\approx 89.3\%$ is obtained, while when sintered at 510 MPa, an average densification of ca. 96.4% is obtained, showing that the pressure has a beneficial impact in reducing the porosity of the solid electrolyte. Pressing for a longer time (15 h instead of 10 min) at the same pressure does not change the overall porosity of the solid electrolyte since the densification reached $\approx 89.3\%$ and 97.3% for the sample pressed at 255 MPa and the one pressed at 510 MPa, respectively. As such, the key parameter for proper densification and reducing the overall porosity remains the pressure.

3.2. Local Thicknesses and Geometric Tortuosity

Unfortunately, the solid electrolytes are not 100% dense which implies that the remaining porosity will cause a higher tortuosity impacting the Li-ion transport and can be the nucleation point to fracture propagation. Geometric tortuosity and local thickness calculations (explanations in the Experimental Section), extracted from the 3D volume collected by FIB-SEM, give an insight into the average length of the lithium-ion path inside the solid electrolyte and the average width of the lithium-ion channel respectively (relevant for lithium-ion transport and effective tortuosity calculation).

For the sample pressed for 10 min at 255 MPa (Table 1), the densification of 89.3% results in a slightly high average tortuosity of around 1.030 (compared to the ideal 100% compacity leading to tortuosity of 1) in the sintering direction. The tortuosity here seems low considering the amount of porosity visible in the 3D images, but this calculation is an average of every possible path connecting the top to the bottom of the investigated volume (ideal Euclidian/straight path of 20 μm and real mean pathway found to be 20.6 μm). When higher pressure is applied (Table 1), the tortuosity drastically decreases to 1.009 (theoretical path of 20 μm , and real mean pathway found to be 20.18 μm). In both cases, the geometric tortuosity parameter seems almost negligible as compared to the ideal tortuosity of 1. Applying the pressure for a longer time does not change the average tortuosity, meaning again that a key parameter for sintering is the pressure more than the time applied.

As such, the geometric tortuosity alone might not be the most adapted metric to assess the Li-ion transport properties,^[22] especially when a small pore will have a negligible impact on the Li-ion pathways, whereas a large pore interconnected through the full volume might drastically influence the Li-ion transport. Indeed, the geometrical tortuosity only describes the length of the lithium path through the volume as it calculates all the possible paths and averages their distances, thus only partially describing Li-ion transport. It is known that physical bottlenecks could hinder the flux of ions and therefore the distribution of the diameter is important. The local thickness measurements can address the description of the bottlenecks by giving the distribution of the diameter of the Li-ion channels. Local thickness measurement can then address better the Li-ion transport hindrance within the solid electrolyte as depicted in **Figure 2**.

For the samples pressed for 10 min at 255 MPa, the average local thickness (or the average distance between pores) is slightly lower than 1 μm whereas increasing the pressure to 510 MPa leads to an average of 1.28 μm in diameter, thus im-

proving the transport by $\approx 30\%$. The same trend can be observed between the samples pressed for 15 h with a 20% increase from 255 MPa to 510 MPa (local thickness increasing from 0.99 to 1.21 μm). Moreover, the distribution of the diameter of the samples sintered at 510 MPa are better spread out toward wider diameter: there is a decrease of small diameters while an increase of the maximum diameters leading us to conclude that the Li-ion transport is better in more sintered sample (higher pressure). However, the effect of a longer sintering time seems to have only limited consequences on the distribution of local thicknesses.

Still based on those analyses, it seems that time has no influence on the sintering properties of the solid electrolyte. Additional parameters are extracted from the 3D investigation to shed light on the role of time on the pressure that should be applied.

3.3. Pores Size Distribution and Geodesic Distance Map Through the Pores

One can represent the porosity on each slice along the three axes X, Y, and Z as shown in **Figure 3**. This representation allows i) to check the homogeneity of pores in the volume, and ii) to understand if the uniaxial pressure is leading to anisotropic distribution of the pores on the electrolyte volume. As discussed previously, the samples sintered at 255 MPa show higher porosity on each slice compared to the samples sintered at 510 MPa (the overall porosity being the average of the porosity of every slice). On the samples pressed at 255 MPa, the variation of porosity between the slices is considerable compared to the samples pressed at 510 MPa suggesting that the pores at 255 MPa are substantially larger and not homogeneously distributed on the overall volume. The same result could be extracted from the representative elementary volume (REV) plots in **Figure S4**, Supporting Information where a smaller REV is found with a $\pm 5\%$ confidence interval for the 10 min pressed samples at 510 MPa compared to the one at 255 MPa. Once again, this indicates a greater pores homogeneity, in size and distribution throughout the volume in the samples sintered at 510 MPa, even with a short pressure time.

When looking closer at the fluctuations of porosity (**Figure 3**) along the three axes or, in other terms, the standard deviation (SD) along each axis, a trend can be seen: on every sample, the lowest fluctuation in porosity is always seen on the Y-axis. This result suggests that there is a greater uniformity along the direction of uniaxial pressure than in the plane of the pellet. This observed behavior is clear once correlated to the cell design. The pressure is applied along the Y-axis, as represented in **Figure 3** and **Figure S3**, Supporting Information, with two stainless steel plates, maintained on the cell by screws. On the X- and Z-axes, the LPS pellet could slightly distort as a polyoxymethylene (POM) disk is used to ensure the electrical isolation of the pellet. Despite the wall thickness of 1 cm and its stiff design, it is possible that the POM disk could be more ductile than the stainless steel plates, leading to a "pressure relaxation" of the SE in the plane of the pellet. At this stage, the difference between the X- and Z-axes is difficult to explain since the sample is a cylinder and no difference is expected between the X- and Z-axes.

So far, we demonstrated that the pressure is a key parameter to control for improving room temperature sintering and

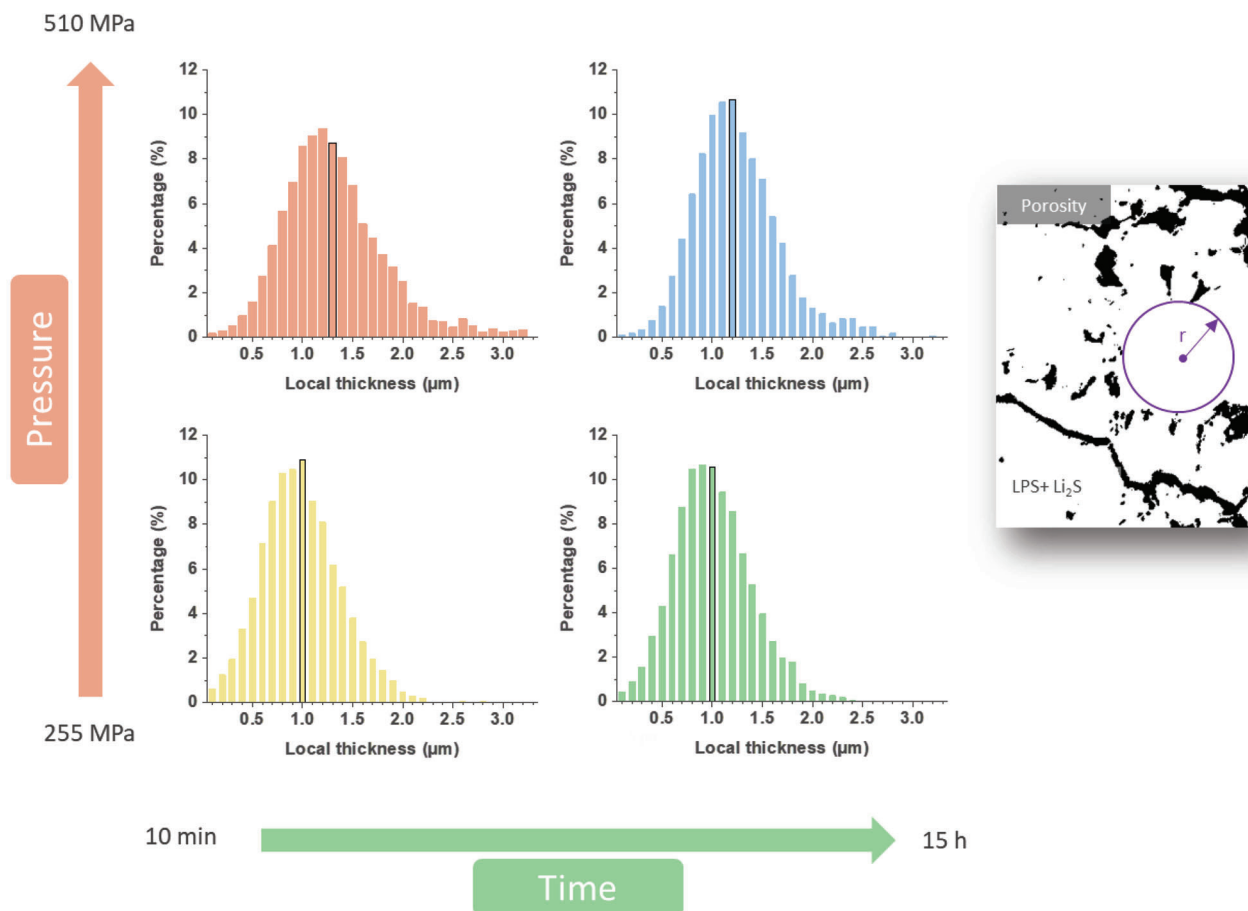


Figure 2. Local thickness histograms and the 2D representation of local thickness measurements. On the histograms, the black outlined bar represents the mean diameter. On the 2D representation, LPS and Li₂S are represented in white and the porosity in black.

that the time seems to have yet a negligible impact. However, looking carefully at the porosity within the volume, we can see some evolution that might have a time dependency. For all samples, two different populations of pores can be detected. The first consists of large pores, superior to tens of μm, not homogeneously distributed in the volume, and that are mainly interconnected and most probably responsible for Li-ion transport hindrance. The second population consists of small unconnected pores (below 1 μm in diameter) spread out through the volume most probably caused by the large particle size distribution of the solid electrolyte powder. Both populations can be seen on every sample (Figures S5 and S6, Supporting Information) even though the proportion of large pores is considerably smaller in the samples pressed at 510 MPa. The main differences here lie in the interconnection of the porosities. The geodesic distance map through the pores is a representation that can help address the dendrites propagation and/or the possibility that Li metal could travel in the solid electrolyte during cell assembly (Figure 4). This geodesic distance map is represented at the end of the video of each sample (Movies S1–S4, Supporting Information, representing the four samples pressed at 255 MPa for 10 min, 255 MPa for 15 h, 510 MPa for 10 min, and 510 MPa for 15 h respectively). As it can be seen from Figure 4, there is a direct connection through the porosity of the sample 255 MPa

– 10 min, guiding the Li, so most probably generating dendrites extremely easily. When we increase the pressure and the time (sample 510 MPa and 15 h), we can see from the geodesic map, that the porosity is not anymore connected through the volume, thus, it is more difficult for the Li to travel within the electrolyte porosity.

The distance calculation starts from the top plane of the volume and propagates through the pores along the Y-axis (simulating the Li-ion transport in the separator in real batteries with lithium metal on the starting top plane). For samples sintered at 255 MPa and the sample sintered at 510 MPa for 10 min, there is a percolation of porosities along the Y-axis that could promote dendrites growth as there is a direct path through pores from the top to the bottom of the separator (Figure 1). Even though the height of the studied volume here is roughly 25 times lower than the separator used in this setup (20 vs 500 μm), it is highly probable that there would be a direct path for lithium to propagate through the porosities network and create short-circuit. Or at least, if a path of more than 20 μm exists at the surface of the separator, it would help to propagate the dendrites faster through the whole volume. However, on the sample sintered at 510 MPa for 15 h, the percolation of pores is lost, and the path of possible Li-metal propagation is drastically restricted. As unbelievable as it can be, this result suggests that sintered solid electrolytes,

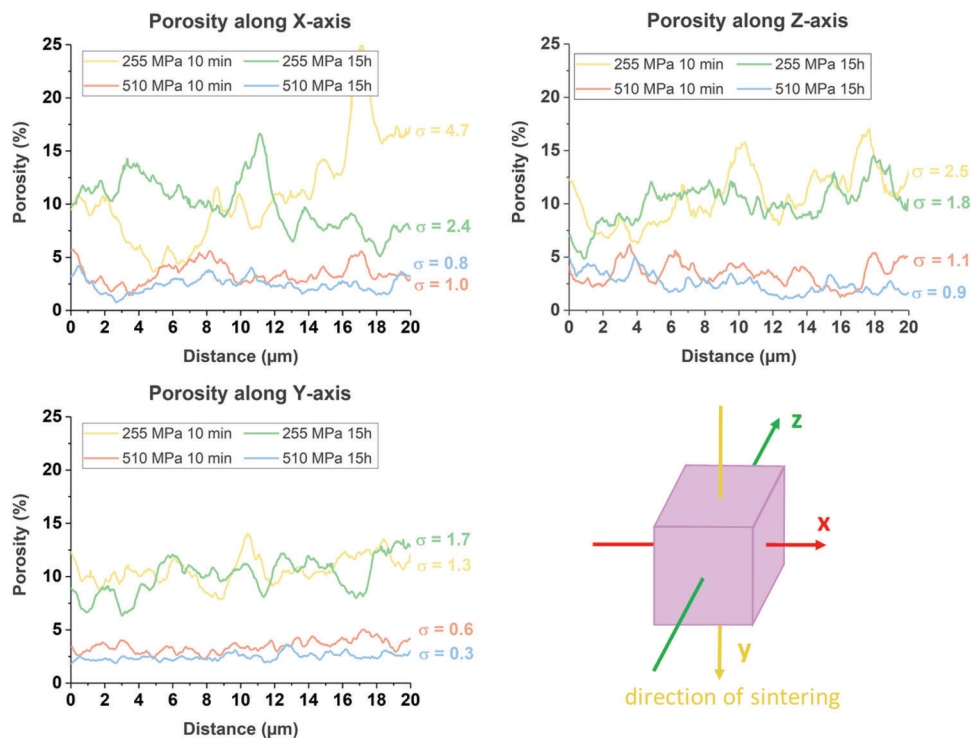


Figure 3. Porosity per slice along the three axes with the standard deviation of porosity, Y-axis toward the center (same axis as the applied pressure), X- and Z-axes toward the edge of the pellet.

with porosity as low as 3.5 vol.% (or 97.5% compacity), could have a direct path for dendrites propagation if the pressure on the solid electrolyte is applied for a short time (only 10 min). This path is suppressed when the solid electrolyte is sintered for a longer time, letting the time to the porosity to re-arrange and close.

Based on the results obtained, we performed a penetration depth profile of Li metal onto the surface of the RT sintered solid electrolyte by fractography. A lithium foil is pressed at 25 MPa (stack pressure later used for plating/stripping tests) on top of LPS pellets previously shaped at 255 MPa for 10 min and 510 MPa for 15 h prior to being investigated by SEM cross-section (Figure 4b–d,f,h). Based on Li metal nature including its low Young modulus and yield strength,^[23] the lithium metal might fill the open pores from the surface to the core of the solid electrolyte. On the sample pressed at 255 MPa for 10 min, the Li penetration has been observed as deep as 82 μm from the Li | LPS interface (Figure 4b,d) while no penetration has been observed on the sample pressed at 510 MPa for 15 h (Figure 4g,h).

Figure 5 gives the pore size distribution for each sample, the cumulative number of pores, and the cumulative volume fraction each class represents. It can be seen that a large number of small pores (low Feret diameter) are present in every sample, but their corresponding volume fraction is negligible in the case of low pressure, and close to 20% of pores of ≈ 1 μm at high pressure and long applied pressure. This is quite promising as small porosities should not really impact the Li-ion transport within the solid electrolyte, however, they can contribute to propagating i) the den-

drates if they start to be formed, and ii) the cracks if stress/strain occurs in this area. At 255 MPa, $\approx 90\%$ of the overall porosity is contained in two distinct pore sizes (higher than 10 μm) when sintered for 10 min and only one pore for the sample sintered for 15 h. Both extremely large porosities are most probably responsible for cell failure (dendrites propagation along the full stack volume) and major Li-ion transport hindrances. When looking at the pellets sintered at 510 MPa for 15 h, a clear microstructural change can be seen with a drastic reduction of big pores. The slope of the cumulative volume fraction of porosity is free from drastic increases. This result implies that the sintering is a slow governing process. To reduce and “close” the big porosities, only time seems to play a role so far, reducing the probability of generating Li dendrite paths.

So far, we demonstrated the impact of pressure and the time this pressure is applied on the solid electrolyte microstructure. However, additional properties are needed to properly determine the parameters improving the electrochemical performance of the solid electrolyte. The second part of the paper is dedicated to assessing the impact of the room temperature sintering parameters on the electrochemical properties of the solid electrolyte as well as looking at the structural properties in the depth of the solid electrolyte during and after sintering.

3.4. Structural Characterization of the Solid Electrolyte

As demonstrated in Figure S1, Supporting Information, LPS (powder) is amorphous with a small amount of Li_2S considered

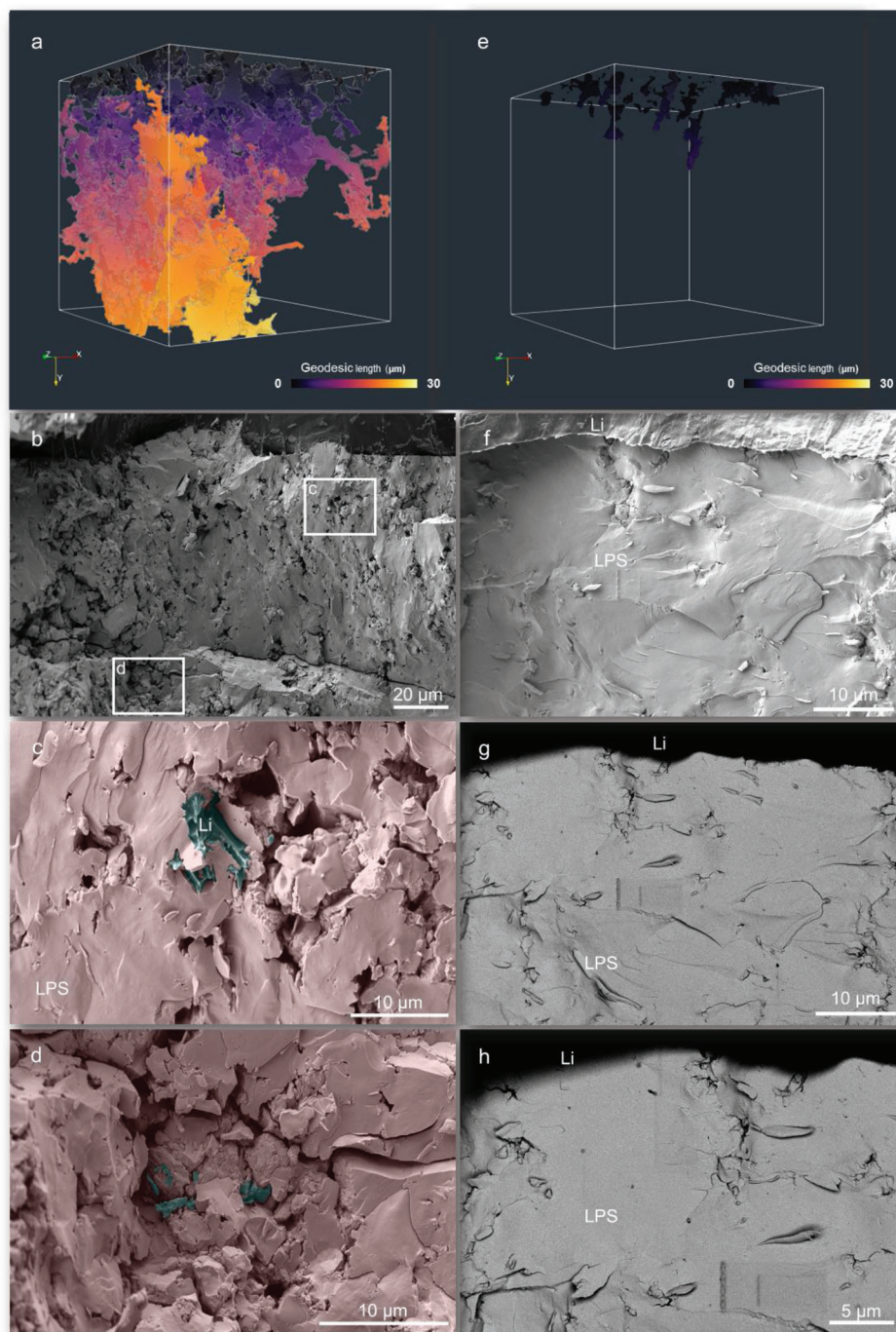


Figure 4. 3D geodesic distance map through the pores and fractography of Li | LPS interface of a–d) for 255 MPa, 10 min and e–h) for 510 MPa, 15 h. Geodesic distance map calculated from the top, propagated to the bottom of the volume. b) Global secondary electron image and. On b) Squares represent the close-up images c,d) SEM images where lithium penetration has been identified. Lithium is represented in blue while LPS is represented in red. Lithium has been confirmed with backscattered electron imaging. f) Global secondary electron image, g,h) close-up secondary and backscattered images respectively highlighting no lithium penetration.

as an impurity. We wanted to know if the sintering parameters (pressure and time) could have an influence on the structural properties of the solid electrolyte, especially in the depth of the solid electrolyte pellet. Thanks to the high penetration of high energy X-rays at a synchrotron source we can track the vertical Y

profile of our four samples by WAXS technique, using a beam size of 5 μm in the vertical direction. It means that for each sample, we collected ≈ 100 diffractograms in the pellet volume, helping to chase local structural changes. Based on our ex situ investigation and whatever the room temperature sintering condition

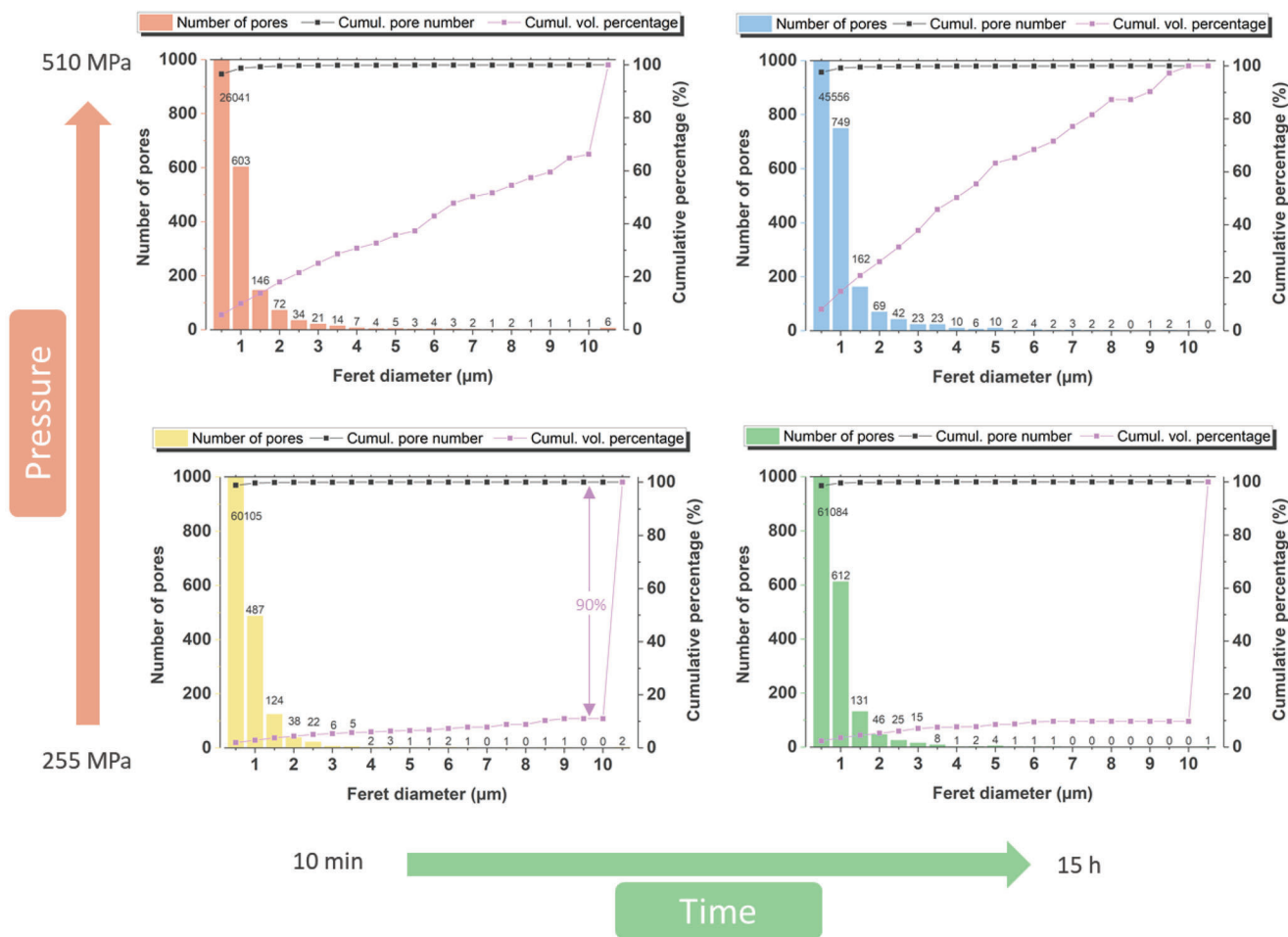


Figure 5. Pore size distribution and cumulative volume fraction for each sample.

used (time and/or pressure) to densify the LPS solid electrolyte, the samples remain all amorphous in the Y position, similarly to the LPS pristine powder. As the structure of the ex situ samples could have evolved with time (relaxation as an example), we performed an in situ experiment by incrementally increasing the applied pressure (from 25 up to 255 MPa) on the sample while following the structural stability. When the sample reached 255 MPa, we still collected the WAXS data as a function of time to mimic the results from long-term sintering. As it can be observed in Figure 6a,b, no modification can be seen on the contour plot representation, nor on the waterfall one showing that the amorphous nature of the solid electrolyte is kept whatever the time/pressure applied.

Based on our data analysis relying on morphological and structural investigation, the best sample is the one having the least remaining porosity and from which there is no connection between the porosity thus, the sample sintered at 510 MPa for 15 h. Now, we performed additional electrochemical tests, mostly the plating/stripping electrochemical test to determine the most important parameters on top of the ionic conductivity.

4. Electrochemical Characterization

4.1. Ionic Transport

In solid-state batteries, the Li-ion transport through the solid electrolyte is ensured by the bulk ionic conductivity and the presence of grain boundaries. Based on the FIB-SEM investigation and on the solid electrolyte nature (amorphous in the whole volume), we logically did not identify any grain boundaries on the samples. The ionic conductivity of LPS was measured by electrochemical impedance spectroscopy (EIS) at different temperatures and the activation energies were extracted from the temperature-dependent Arrhenius plot as shown in Figure 7a. The activation energy is similar for all the samples $\approx 0.37 \pm 0.01$ eV and in good agreement with the literature.^[24,25] This result is somehow logical as it is not expected that the pressure/time could have an impact on the transport phenomenon occurring in the electrolyte. The high-frequency (HF) processes corresponding to ionic transport (Figure S7, Supporting Information) were fitted using the equivalent circuit presented in Figure S8a, Supporting

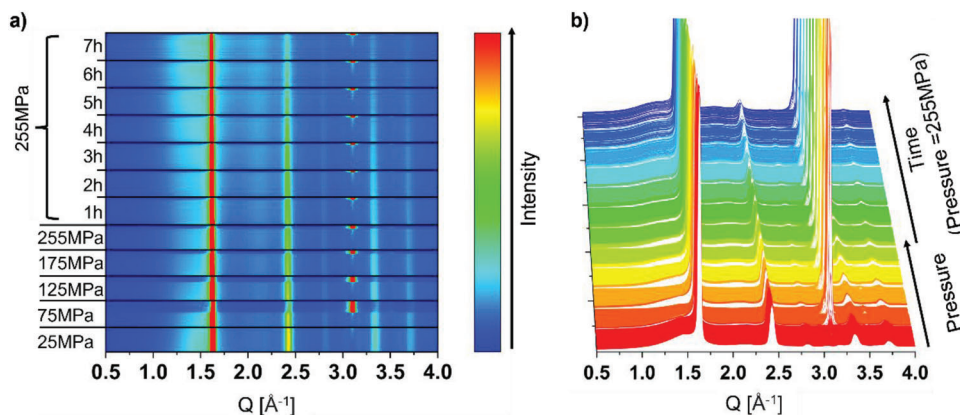


Figure 6. a) Contour plot representation of the X-ray diffractograms collected at the synchrotron source (ID31 – ESRF) during an in situ room temperature sintering test (along the Y-axis of the pellet), the color indicates a change in the intensity of the diffractogram; b) the waterfall representation of the same experiment, each color indicated a change in the pressure and/or time. All the peaks observed in the diffractograms are related to the sample holder (Either stainless steel, POM disk, or pouch bag).

Information. The calculated capacitance of the high frequency (C_{HF}) phenomenon is determined according to Equation (1):^[26]

$$C_{HF} = (Q_{HF})^{\frac{1}{\alpha}} \times (R_{HF})^{\frac{1-\alpha}{\alpha}} \quad (1)$$

where Q_{HF} represents the constant phase element parameter (CPE) in $F s^{(\alpha-1)}$ and α is a dimensionless parameter varying between 0 and 1.

Above 30 °C, the semi-circle at HF is not properly defined making it difficult to accurately estimate the value of the capacitance due to the large error bar (Figure S8b, Supporting Information is the equivalent circuit when the semi-circle is not visible). In the temperature range (30 and –30 °C), C_{HF} for all the samples is constant ($\approx 5.4 \pm 0.6 \times 10^{-11}$ F). This value corresponds to the bulk transport in the solid electrolyte as already reported in the literature.^[27] Even at low temperatures, the contribution of the grain boundaries is not visible (confirmed by FIB-SEM) in

agreement with the amorphous character of the solid electrolyte as seen by in situ WAXS.

As mentioned, the ionic conductivity is quite often linked to the compacity of the solid electrolyte. Indeed, a highly porous material will present a poor ionic conductivity that will increase if the material is properly densified. However, a threshold exists, where at some point and despite the presence of some porosity, the ionic conductivity will be roughly the same.^[28] As can be seen in Figure 7a, pressure and time applied on LPS powder seem to have little influence on the obtained ionic conductivity showing that, after 10 min at 255 MPa, we reach the threshold of good conductivities with remaining porosity. However, with lower pressure and (thus higher porosity content), we can see that the ionic conductivity dropped (Figure 7b). Based on this result, it means that the ionic conductivity remains the same once we reach the threshold (here around 200 MPa) and so whatever the remaining porosity content in the sample.

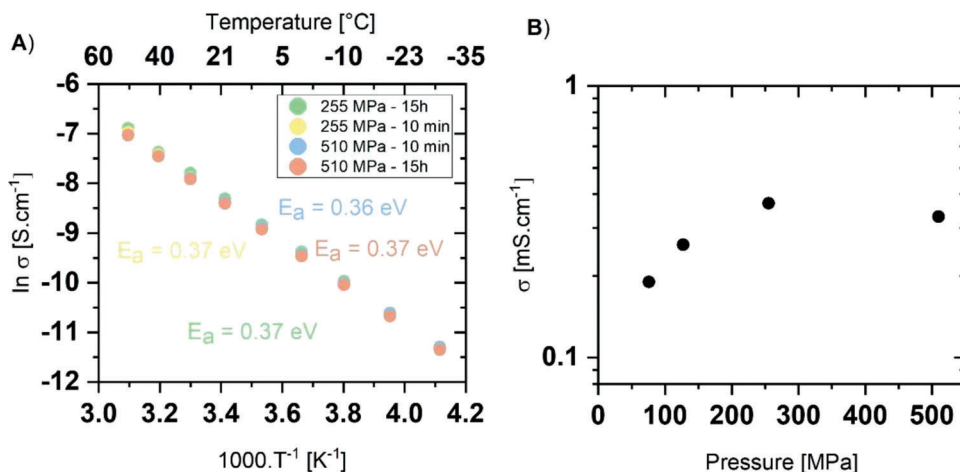


Figure 7. a) Temperature dependence of the ionic conductivity of LPS as a function of the shaping parameter (time and pressure). The activation energy was obtained from the linear regression fit of the Arrhenius plot; b) Ionic conductivities recorded as a function of the pressure applied, for a sample pressed during 10 min.

Table 2. Summary of the ionic conductivities and the relation to the porosity for the four samples. TA stands for conductivity measured with the thickness taken before measurement, whereas TB stands for the thickness measured after the EIS measurement.

	255 MPa, 10 min	255 MPa, 15 h	510 MPa, 10 min	510 MPa, 15 h
Porosity volume fraction [%] estimated by FIB-SEM	10.5	10.0	3.5	2.4
Ionic conductivity [$\text{mS}\cdot\text{cm}^{-1}$] TB	0.36	0.32	0.30	0.29
Ionic conductivity [$\text{mS}\cdot\text{cm}^{-1}$] TA	0.32	0.29	0.30	0.29

Once the threshold is reached, the ionic conductivities are roughly the same. Slight differences might be coming from i) the estimation of the thickness of the pellet causing a non-negligible error bar on the measurement and/or ii) the relaxation of the sample during the measurement. For the latter, the thickness measurement can be performed before the experience, or after the measurement. To identify if this parameter has an influence on the overall ionic conductivity, we measured the sample before (before the measurement, respectively after 10 min or 15 h applied pressure) and after ionic conductivity measurement (where the cells are closed with the fabrication pressure and are opened after 15 days). The results are presented in Figure S9, Supporting Information. If one compares the ionic conductivity as a function of when the thickness is measured (before or after the EIS measurement), we can see that after the EIS measurement, the difference between all the samples is drastically reduced compared to the thickness measurement performed before the measurement. We notice that for the samples pressed at 510 MPa, the thickness measured before and after the EIS experiment does not change, independently of the time at which the pressure was applied. On the other hand, at 255 MPa, the thickness changes significantly. This behavior, which we ascribed to a relaxation process, can be linked to the low Young's modulus of the LPS solid electrolyte of 25 GPa,^[28] indicating that if a cell is closed under pressure, the sintering process might still continue. Sakuda et al.^[28] note that the ionic conductivities do not increase after a certain fabrication pressure while the porosity seems to decrease, indicating that the pressure applied by the cell can still affect the morphology of the solid electrolyte. Furthermore, it has been observed for the amorphous electrolyte that, if sufficient fabrication pressure is applied, a small stacking pressure (< 50 MPa) is sufficient to obtain a stable ionic conductivity value.^[17] Therefore, it is important to measure the thickness before and after the experiment, especially when the applied stacking pressure is high. The results of the ionic conductivity as well as the morphology of the samples are all summarized in **Table 2**. Another parameter that can be extracted from the thickness measurement is the porosity of the pellet (Note S1, Supporting Information). Those results agree with the one determined by FIB-SEM (Note S1 and Table S1, Supporting Information).

4.2. Resistance Evolution

As already discussed, the sintering can “continue” once the cell is closed at a dedicated pressure, as we demonstrated with the evolution of the thickness of the pellet. Thus, we followed the evolution of the ionic resistance as a function of time for the four samples during 180 h, performing an EIS measurement every

10 min. As shown in **Figure 8**, we can see for all samples that the ionic resistance is increasing as a function of time in a non-linear manner (following more a logarithm profile, Figure 8a). First, there is a sharp increase of the resistance during the first 25 h, followed by a “stabilization”.

Several reasons can explain this phenomenon: i) The evolution of the porosity inside the sample since the cell is closed at a certain pressure, as we demonstrated that the thickness evolves with time, ii) a “distortion” of the pellet due to the design of the cell (POM disk), and/or iii) a surface reaction of the solid electrolyte in contact with stainless-steel. As can be seen, hypotheses (i) and (ii) are both linked to the porosity evolution whereas hypothesis (iii) is related to surface reaction. Generally, when a surface reaction is occurring in the cell, the resistance follows a linear trend versus the square root of time. This representation is used to describe diffusion-controlled solid-state reactions, especially the evolution of the solid electrolyte interphase (SEI).^[29,30] In the present case (Figure 8b), we can see that the evolution of the resistance as a function of the square root of time is not fully linear showing that surface reaction cannot solely explain the evolution of the resistance. Thus, the two pre-cited hypotheses are most probably valid.

We attempted a linear regression on the curves extracted from Figure 8b. As it can be seen in Figure S10, Supporting Information, two linear regressions are needed to fit the curve signifying that two different processes are happening. We believe that the first one, having a sharper slope, is linked to the relaxation of the porosity, which occurs relatively fast when the cell is closed, whereas the second one is seen as the surface reaction with the stainless steel. In any case, the change of ionic conductivities is $\approx 10\%$ at the end of the measurement for all samples, exhibiting the same trend.

4.3. Li Plating/Stripping

A last parameter that we assessed while investigating the room temperature sintering of the solid electrolyte is the ability to plate/strip Li using different currents (**Figure 9** and Figure S11, Supporting Information). It consists of applying a constant current during five cycles and progressively increasing this current for the next five cycles. Once the five currents are measured, the cell is back to the first applied current. Depending on the porosity of the solid electrolyte, the Li plating/stripping test can also help determine the critical current at which the dendrites are formed and propagated.

Some cells were prone to short circuits even before starting the cell. This may be caused by i) the pellet thickness being less important at higher pressure (denser sample), and/or ii) the

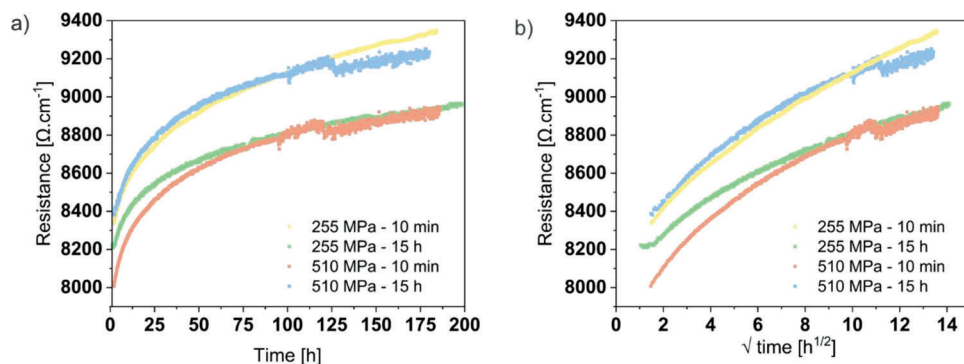


Figure 8. Evolution of the ionic resistance as a) a function of time and b) a function of the square root of time for all four samples.

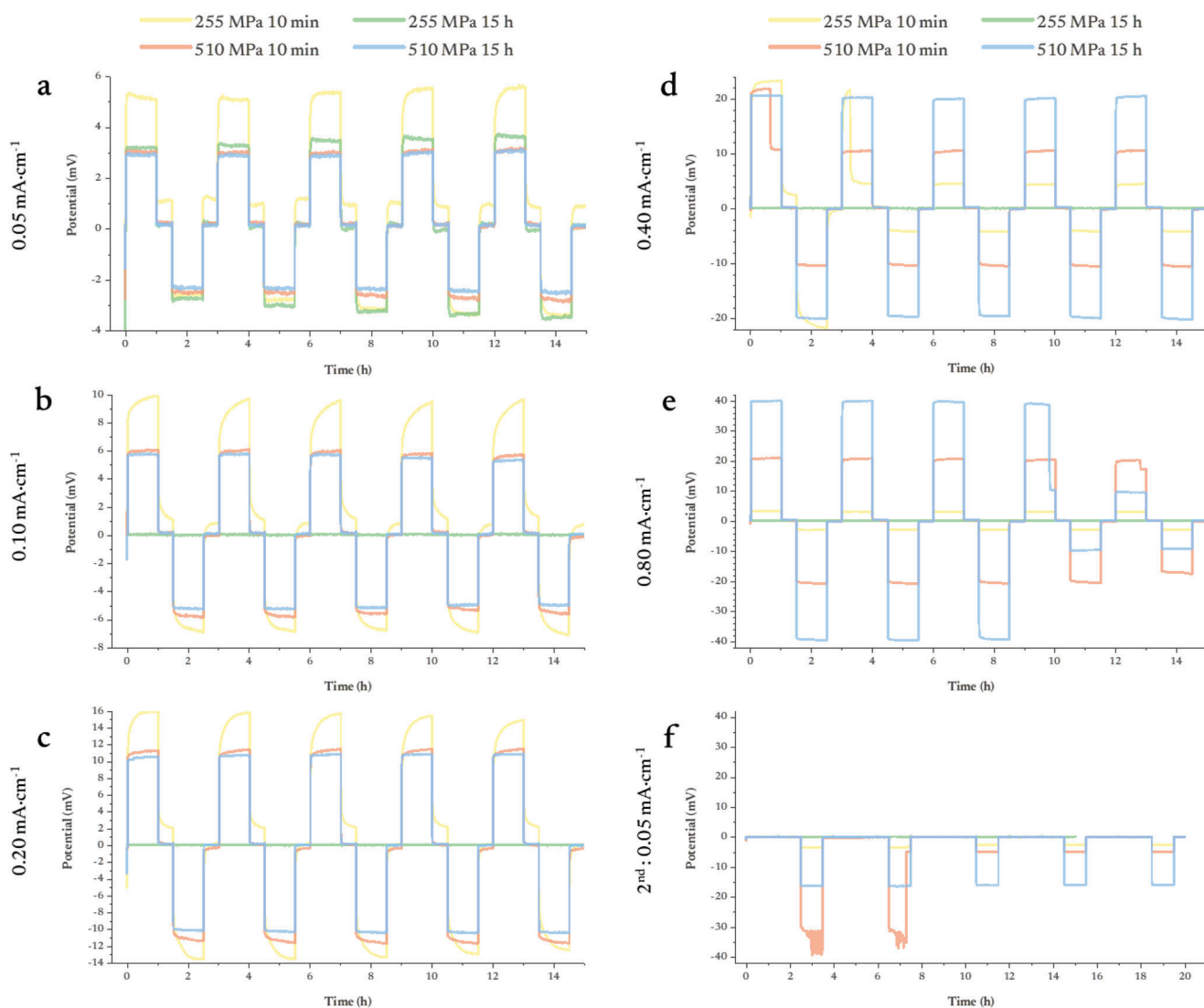


Figure 9. Lithium plating/stripping experiment applied on the two sintered solid electrolytes for 10 min. The current density is corresponding to a) 0.05, b) 0.10, c) 0.2, d) 0.4, and e) 0.8 mA cm⁻² and back to f) 0.05 mA cm⁻².

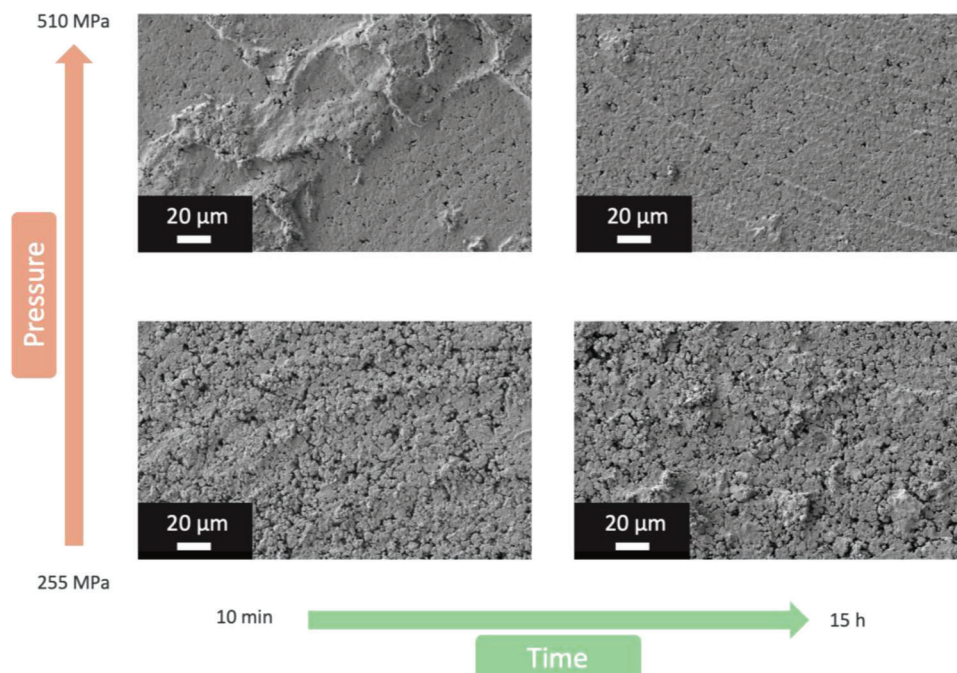


Figure 10. Secondary electron images showing the surface rugosity of the pellet after the sintering process applied.

dendrites propagation through the edge of the POM disk linked to a smaller pellet.

At the lowest current density (0.05 mA cm^{-2}), we observe the typical behavior of Li plating/stripping, with positive and negative polarization (less than 5 mV). The polarization follows the porosity of the samples, it is less important for the denser materials (15 h at 510 MPa) and higher for the most porous ones (255 MPa and 10 min). When applying a higher current (0.1 mA cm^{-2}), the polarization splitting between the less dense and denser materials intensifies, leading to higher polarization for the 255 MPa and 10 min sample and surprisingly the sample sintered at 255 MPa for 15 h short-circuited. One reason for the short-circuited behavior could be the dendrites, being easier to propagate in the less dense samples, as seen by the geodesic maps (Figure 4). The overpotential continues to increase for the sample pressed at 255 MPa for 10 min and a noticeable change can be seen in the shape of the polarization curves. Indeed, we can see a tail at the end of the potentiostatic plateau when the current is increasing, characteristic of contact loss.^[11,20] At the lowest applied current, the plating/stripping test follows an ohmic behavior, but when the current is increased, the ohmic behavior is lost. This phenomenon is more pronounced for the samples sintered at lower pressure. Several reasons can explain this behavior: i) the surface contact between the Li counter electrode and the solid electrode pellet, as the surface rugosity plays a role (Figure 10); ii) the degradation products generated at the interface once the Li is in contact with the solid electrolyte pellet; iii) once the Li is plated or stripped, mossy Li is deposited at the surface and compete with fresh Li; fresh Li does not suffer any polarization and the mossy one is covered most probably with insulating surface decomposition products (Li_2S , Li_3P , etc.), and, iv) the possible cracks/pores that can develop between the Li metal layer and the solid electrolyte caused by the inhomogeneous Li plating/stripping. We al-

ready discussed the first two points and demonstrated that they play a key role in the noticed polarization. For points (iii) and (iv), both can indeed play a role since the contact at the interface is always a weak point in solid-state batteries; there is no doubt that Li plating/stripping would not be homogeneous, and that mossy/fresh Li will compete. Consequently, voids will be created at the interface between the solid electrolyte and the Li metal counter electrode.

Continuing increasing the current (0.2 mA cm^{-2}), the trend is the same for the three remaining samples, except that the polarization continues to increase. At the current of 0.4 mA cm^{-2} , the sample sintered at 255 MPa for 10 min has a high polarization before breaking down, showing dendrite formation. The same observation is done on the sample sintered at 510 MPa for 10 min: the drop from 22 to 10 mV corresponds to the formation of a dendrite.

Increasing the current to 0.8 mA cm^{-2} , the denser sample (510 MPa for 15 h) is the only sample to withhold such current but sees its polarization suddenly decreasing after the fourth cycle, showing a dendrite formation. At this point, except for the sample sintered at 255 MPa for 15 h prematurely short-circuited at 0.1 mA cm^{-2} , the three remaining samples still continue to plate/strip to higher current but signs of failure start to appear in the form of a drop in the polarization curves at different current depending on their sintering parameters. Once back to the starting current, all samples either short-circuited or are no plating/stripping in a reversible manner.

The understanding of plating/stripping behavior is far from trivial, but some tendencies can be discussed. The denser samples, sintered at 510 MPa, are less prone to dendrites formation at low current density than their counterpart sintered at 255 MPa, which agrees with the geodesic map showing that the porosities are connected through the full volume of the solid electrolyte,

guiding the dendrites. Unsurprisingly, the samples sintered for a longer time (15 h instead of 10 min) leads to later dendrite formation, which is in coherence with the previous fractography observation. The open porosity has a direct impact on the critical current density a cell can reach against lithium metal. A stack pressure of 25 MPa is sufficient to creep lithium inside the pores and subsequently increase the active surface between LPS and lithium metal, proportionally to open porosity.

5. Conclusion

Through this paper, we gathered information about structure, morphology, and electrochemistry to understand the impact of pressure and time this pressure is applied on the sintering of Li_3PS_4 amorphous solid electrolyte. We first demonstrated that pressure is a key parameter to reduce the overall porosity whereas the time this pressure is applied has an impact on the overall porosity (their dimension) and on the pore's connection. Whatever the samples and the sintering parameters used, they all possess the same ionic conductivity meaning that already with $\approx 10\%$ of remaining porosity, we reach a threshold. Thus, one cannot only rely on ionic conductivity for selecting the best solid electrolyte. Indeed, the distribution of the porosity within the sample seems to be the most crucial parameter since it can guide the dendrites formation and be responsible for mechanical fracture. The best sintering condition, is thus, a high pressure applied (in the present case 510 MPa) to avoid connection of the porosity through the full solid electrolyte volume, but also a longer sintering time since the porosity remains small (so in total, there are fewer pores in the samples) leading to less fractures/dendrite propagation.

6. Experimental Section

Electrolyte Synthesis: All the products were manipulated in a glovebox filled with argon. The solid-electrolyte was obtained through ball-milling synthesis. Lithium sulfide (Li_2S , Sigma-Aldrich 99.98%) and phosphorus pentasulfide (P_2S_5 , Sigma-Aldrich 99%) were weighed for a 1.5 g batch (75% Li_2S –25% P_2S_5 molar ratio) and put in a ZrO_2 jar with 5 mm ZrO_2 balls. The powder mixture was milled (Fritsch, planetary mill apparatus Pulverisette 7) at 510 rpm for 360 cycles (5 min active and 15 min rest).

Pellets Fabrication: The solid electrolyte was shaped using a homemade cell already developed in the laboratory as described.^[24] The cell consisted of two stainless steel pressing plungers and a 7 mm POM cylinder that allowed electrical insulation of the two plates. Roughly 30 mg of LPS was added to the cell cavity, then, the cell was closed with the top plunger and the pressure was applied on the powder directly. The pellets were sintered at a pressure of 255 and 510 MPa at different times.

Estimation of Initial Particle Size: A small amount of LPS powder was placed on an SEM stub prior to being measured at a Zeiss Ultra 55 SEM using 2 kV. Ten images were taken in random locations using a backscattered electron detector. The obtained SEM images were segmented using Ilastik software.^[31] The classifier was trained with annotations until the output segmentation seemed acceptable with minimum error in the phase identification. The segmentation images were then imported into Fiji software.^[32,33] A distance transform watershed from Morpholibj^[34] (Borgefors model) was performed to separate agglomerate particles into smaller elementary particles. Once the threshold was applied, the images were successively eroded using morphological filters from Morpholibj (erosion, disk kernel of radius 1) and then dilated using the built-in binary operation of Fiji (dilate, iteration 1, count 1). This step ensured to

disconnect all the particles previously separated with the watershed operation. A histogram of the Feret diameter was calculated from the analysis of every particle using the in-built Fiji analyzer.

FIB-SEM Preparation and Data Acquisition: The sample preparations and the FIB-SEM tomographies were performed using a Zeiss Crossbeam 550.

A $21 \times 21 \mu\text{m}^2$ area of interest was protected by a 2 μm -thick layer of platinum deposited on the surface (30 kV – 3 nA). To ensure a fair comparison between the pellets, the area of interest was chosen at a radius of 0.5 mm from the center of the pellets. Fiducial markers were etched on the platinum and then filled with a carbon deposit (30 kV – 50 pA). Those markers both served for the alignment correction of the successive imaging as well as the milling position. A 2 μm -thick carbon film was deposited to protect the surface of the sample (30 kV – 3 nA). 30 μm -deep trenches around the area of interest were dug to open the cross-section of the electrolyte and reduce the shadowing effect during secondary electron imaging (30 kV – 30 nA). The cross-section was polished at the aperture used for further acquisition (30 kV – 1.5 nA) to obtain a flat surface. Hundreds of consecutive images were acquired both with secondary and backscattered electron detectors with a 2 nA current and 2 kV electron acceleration. Volumes with 20 nm cubic voxels were then obtained for all tomography images.

Data Pre-Processing: Image sequences were stacked, registered, and cropped using Fiji software and its plugin Multistackreg. From the plugin, a transformation matrix was extracted. The shearing due to the 54° angle of the electron beam was corrected using the previously extracted transformation matrix with an in-house Python code. The intensity gradient on secondary electron images was removed with the Xlib.^[35] plugin in Fiji. Secondary electron and backscattered electron images were merged and exported as a .h5 file as a 4D stack. This method allowed the authors to withhold both Z-contrast and topographic contrast in each voxel.

Image segmentation was done with Ilastik software. The classifier was trained with annotations until the output segmentation seemed acceptable with minimum error in the phase identification.

Computational Procedures – General Quantification: The volume fraction of each phase was calculated using the Morpholibj plugin's function "Analyze Region 3D". The geodesic distance map was calculated with the Morpholibj plugin with a marker on the top of the volume (surface of the sample).

The tortuosity was calculated with the ImageJ plugin made by Roque and Costa, 2020.^[36] The calculation was done in 3D while the propagation was set to 6 near neighbor voxel.

The local thickness^[37] of the LPS constrained by the porosity was calculated in Fiji. Histograms were calculated from the 3D local thickness representation. The local thickness lookup table adapted the thickness maxima between all samples. Pore size distribution was calculated using the 3D Suite^[38] in Fiji.

Representative elementary volume was calculated with an in-house Python code, inspired by Singh et al.^[39]

Electrochemical Methods: The pellet was prepared as described above. The cells were closed at the pressure applied during the sintering of the pellet (255 or 510 MPa). Electrochemical impedance spectroscopy for LPS alone was measured in a controlled climate chamber (CTS) with a Biologic VMP 300 potentiostat at open circuit potential (OCP). For the ionic conductivity measurement, EIS was recorded from 25 to 50 $^\circ\text{C}$ then from 50 to -30°C , and the measurement ended with a last measurement at 20 $^\circ\text{C}$. A program with a 10 $^\circ\text{C}$ step except for the first change from 25 to 30 $^\circ\text{C}$ was used. The potential amplitude for the EIS measurement was adapted based on the EIS response between 20 and 80 mV.

The evolution of the ionic conductivity as a function of time was evaluated at 25 $^\circ\text{C}$ with a perturbation of 50 mV. The frequency ranged from 7 MHz to 1 Hz. All the fits were performed using the RelaxIS 3 software.

For the plating-stripping configuration (stainless steel/Li/LPS/Li/stainless steel), the Li was prepared as follows: two 4 mm disks of lithium (50 μm thickness) were cut and placed in the center of the 7 mm diameter pellet. The cell was closed and a pressure of ≈ 25 MPa was applied for 10 min before tightening the screws.

The galvanostatic cycling with potential limitation (GCPL) method was used to plate and strip the lithium. For a typical sequence, the current

was imposed in positive mode (plate) and then reversed in negative mode (strip) and was repeated five times with 30 min OCP between each current swap. After each sequence, the current was increased to evaluate the critical current density for the dendrite's formation.

X-Ray Diffraction Measurement at ESRF Synchrotron: The high-energy X-ray beam (75 keV) was focused on the solid electrolyte pellet (beam size $\approx 5 \times 20 \mu\text{m}^2$, vertical \times horizontal). The scattered signal was collected using a Dectris Pilatus CdTe 2 M detector. The energy, detector distance, and tilts were calibrated using a standard CeO_2 powder (NIST), and the 2D diffraction patterns were reduced to the presented 1D curves using the pyFAI software package.^[40]

Supporting Information

Supporting Information is available from the Wiley Online Library or from the author.

Acknowledgements

P.P. and A.F.-M. contributed equally to this work. The authors would like to thank ESRF for the provision of the beamtime at the ID31 beamline. Beamtime at the ESRF was granted within the Battery Pilot Hub MA4929 "multi-scale multi-techniques towards a European battery hub". The authors would also like to thank Thomas David for his insights and precious advice on FIB-SEM acquisition and data treatment. Part of this work, carried out on the Platform of Nanocharacterization (PFNC), was supported by the "Recherche Technologique de Base", program of the French National Research Agency (ANR). ANR Grant OpInSolid is also acknowledged for financial support of this work. Special acknowledgements are made to open software like Fiji and Ilastik and their incredible developers.

Conflict of Interest

The authors declare no conflict of interest.

Data Availability Statement

The data that support the findings of this study are available from the corresponding author upon reasonable request.

Keywords

electrochemical impedance spectroscopy, FIB-SEM tomography, ionic conductivity, lithium stripping, microstructure, room temperature sintering, solid-state batteries

Received: September 6, 2023
Published online:

- [1] S. Randau, D. A. Weber, O. Kötzer, R. Koerver, P. Braun, A. Weber, E. Ivers-Tiffée, T. Adermann, J. Kulisch, W. G. Zeier, F. H. Richter, J. Janek, *Nat. Energy* **2020**, *5*, 259.
- [2] P. Albertus, S. Babinec, S. Litzelman, A. Newman, *Nat. Energy* **2018**, *3*, 16.
- [3] L. R. Mangani, C. Villevieille, *J. Mater. Chem. A* **2020**, *8*, 10150.
- [4] H. Liu, Y. Liang, C. Wang, D. Li, X. Yan, C.-W. Nan, L.-Z. Fan, *Adv. Mater.* **2022**, 2206013, <https://doi.org/10.1002/adma.202206013>.
- [5] X. Lu, A. Bertei, D. P. Finegan, C. Tan, S. R. Daemi, J. S. Weaving, K. B. O'regan, T. M. M. Heenan, G. Hinds, E. Kendrick, D. J. L. Brett, P. R. Shearing, *Nat. Commun.* **2020**, *11*, 2079.
- [6] B. T. Habte, F. Jiang, *Solid State Ionics* **2018**, *314*, 81.
- [7] T. Ates, A. Neumann, T. Danner, A. Latz, M. Zarrabeitia, D. Stepien, A. Varzi, S. Passerini, *Adv. Sci.* **2022**, *9*, 2105234.
- [8] T. Shi, Y.-Q. Zhang, Q. Tu, Y. Wang, M. C. Scott, G. Ceder, *J. Mater. Chem. A* **2020**, *8*, 17399.
- [9] H. Al-Salih, M. S. E. Houache, E. A. Baranova, Y. Abu-Lebdeh, *Adv. Energy Sustainability Res.* **2022**, *3*, 2200032.
- [10] C. Doerrer, I. Capone, S. Narayanan, J. Liu, C. R. M. Grovenor, M. Pasta, P. S. Grant, *ACS Appl. Mater. Interfaces* **2021**, *13*, 37809.
- [11] D. K. Singh, A. Henss, B. Mogwitz, A. Gautam, J. Horn, T. Krauskopf, S. Burkhardt, J. Sann, F. H. Richter, J. Janek, *Cell Rep. Phys. Sci.* **2022**, *3*, 101043.
- [12] R. Garcia-Mendez, F. Mizuno, R. Zhang, T. S. Arthur, J. Sakamoto, *Electrochim. Acta* **2017**, *237*, 144.
- [13] R. Garcia-Mendez, J. G. Smith, J. C. Neufeind, D. J. Siegel, J. Sakamoto, *Adv. Energy Mater.* **2020**, *10*, 2000335.
- [14] H. Tsukasaki, S. Mori, S. Shiotani, H. Yamamura, *Solid State Ionics* **2018**, *317*, 122.
- [15] H. Tsukasaki, M. Otoyama, Y. Mori, S. Mori, H. Morimoto, A. Hayashi, M. Tatsumisago, *J. Power Sources* **2017**, *367*, 42.
- [16] M. Kodama, A. Ohashi, S. Hirai, *J. Power Sources Adv.* **2020**, *4*, 100019.
- [17] M. Cronau, M. Szabo, C. König, T. B. Wassermann, B. Roling, *ACS Energy Lett.* **2021**, *6*, 3072.
- [18] J.-M. Doux, Y. Yang, D. H. S. Tan, H. Nguyen, E. A. Wu, X. Wang, A. Banerjee, Y. S. Meng, *J. Mater. Chem. A* **2020**, *8*, 5049.
- [19] M. Otoyama, M. Suyama, C. Hotehama, H. Kowada, Y. Takeda, K. Ito, A. Sakuda, M. Tatsumisago, A. Hayashi, *ACS Appl. Mater. Interfaces* **2021**, *13*, 5000.
- [20] J. Kasemchainan, S. Zekoll, D. Spencer Jolly, Z. Ning, G. O. Hartley, J. Marrow, P. G. Bruce, *Nat. Mater.* **2019**, *18*, 1105.
- [21] Z. Ning, D. S. Jolly, G. Li, R. De Meyere, S. D. Pu, Y. Chen, J. Kasemchainan, J. Ihli, C. Gong, B. Liu, D. L. R. Melvin, A. Bonnin, O. Magdysyuk, P. Adamson, G. O. Hartley, C. W. Monroe, T. J. Marrow, P. G. Bruce, *Nat. Mater.* **2021**, *20*, 1121.
- [22] J. Janek, W. G. Zeier, *Nat. Energy* **2016**, *1*, 16141.
- [23] C. Xu, Z. Ahmad, A. Aryanfar, V. Viswanathan, J. R. Greer, *Proc. Natl. Acad. Sci. U. S. A.* **2017**, *114*, 57.
- [24] X. Wu, M. El Kazzi, C. Villevieille, *J. Electroceram.* **2017**, *38*, 207.
- [25] A. Hayashi, S. Hama, H. Morimoto, M. Tatsumisago, T. Minami, *J. Am. Ceram. Soc.* **2001**, *84*, 477.
- [26] C. H. Hsu, F. Mansfeld, *Corrosion* **2001**, *57*, 747.
- [27] J. T. S. Irvine, D. C. Sinclair, A. R. E. West, *Adv. Mater.* **1990**, *2*, 132.
- [28] A. Sakuda, A. Hayashi, M. Tatsumisago, *Sci. Rep.* **2013**, *3*, 2261.
- [29] S. Wenzel, T. Leichtweiss, D. Krüger, J. Sann, J. Janek, *Solid State Ionics* **2015**, *278*, 98.
- [30] S. Wenzel, S. J. Sedlmaier, C. Dietrich, W. G. Zeier, J. Janek, *Solid State Ionics* **2018**, *318*, 102.
- [31] S. Berg, D. Kutra, T. Kroeger, C. N. Straehle, B. X. Kausler, C. Haubold, M. Schiegg, J. Ales, T. Beier, M. Rudy, K. Eren, J. I. Cervantes, B. Xu, F. Beuttenmueller, A. Wolny, C. Zhang, U. Koethe, F. A. Hamprecht, A. I. Kreshuk, *Nat. Methods* **2019**, *16*, 1226.
- [32] C. A. Schneider, W. S. Rasband, K. W. Eliceiri, *Nat. Methods* **2012**, *9*, 671.
- [33] J. Schindelin, I. Arganda-Carreras, E. Frise, V. Kaynig, M. Longair, T. Pietzsch, S. Preibisch, C. Rueden, S. Saalfeld, B. Schmid, J.-Y. Tinevez, D. J. White, V. Hartenstein, K. Eliceiri, P. Tomancak, A. F. Cardona, *Nat. Methods* **2012**, *9*, 676.
- [34] D. Legland, I. Arganda-Carreras, P. Andrey, *Bioinformatics* **2016**, *32*, 3532.
- [35] Xlib. ImageJ Wiki, <https://imagej.github.io/plugins/xlib/index> (accessed: November 2022).

- [36] W. L. Roque, R. R. A. Costa, *Appl. Comput. Geosci.* **2020**, *5*, 100019.
- [37] R. Dougherty, K.-H. Kunzelmann, *Microsc. Microanal.* **2007**, *13*, 1678.
- [38] J. Ollion, J. Cochenec, F. Loll, C. Escudé, T. Boudier, *Bioinformatics* **2013**, *29*, 1840.
- [39] A. Singh, K. Regenauer-Lieb, S. D. C. Walsh, R. T. Armstrong, J. J. M. Van Griethuysen, P. Mostaghimi, *Geophys. Res. Lett.* **2020**, *47*, 2020GL088594.
- [40] G. Ashiotis, A. Deschildre, Z. Nawaz, J. P. Wright, D. Karkoulis, F. E. Picca, J. Kieffer, *J. Appl. Crystallogr.* **2015**, *48*, 510.